Gate-switchable SQUID based on Dirac semimetal Cd_3As_2 nanowires

Na Li,[1] Chun-Guang Chu,[1] Jing-Jing Chen,[2,3,*] An-Qi Wang,[1,†] Zhen-Bing Tan,[2,3] Zhen-Cun Pan,[1] Zhao-Hui Chen,[1] Da-Peng Yu,[2,3] and Zhi-Min Liao[1,4,‡]

[1]*State Key Laboratory for Mesoscopic Physics and Frontiers Science Center for Nano-optoelectronics, School of Physics, Peking University, Beijing 100871, China*

[2]*Shenzhen Institute for Quantum Science and Engineering, Southern University of Science and Technology, Shenzhen 518055, China*

[3]*International Quantum Academy, Shenzhen 518055, China*

[4]*Hefei National Laboratory, Hefei 230088, China*

(Received 8 November 2022; accepted 5 June 2023; published 21 June 2023)

Topological semimetal nanowires in proximity with *s*-wave superconductors are promising for Majorana-based topological quantum computers. To braid the Majorana modes, an interconnected nanowire network coupled to superconductor islands is required. Here, we have fabricated the nanostructures based on two Dirac semimetal Cd_3As_2 nanowires connected in parallel to form a symmetric superconducting quantum interference device (SQUID). A proximity-induced superconducting state is achieved in the SQUID, and its gate voltage and magnetic field dependence are investigated. It is found that the supercurrent can be switched on/off by modulating the gate voltage, behaving as a supercurrent field-effect transistor. Under an out-of-plane magnetic field, the SQUID shows an anomalous magnetic field -enhanced superconductivity behavior near the Dirac point. An in-plane magnetic field experiment shows a typical π periodicity of a critical current with the rotation angle. Our work realizes the implementation and characterization of nanowire SQUID structures, which is a significant step toward integrating Dirac semimetal nanowires into scalable superconducting networks for braiding non-Abelian quantum states.

DOI: 10.1103/PhysRevB.107.224513

I. INTRODUCTION

The idea of using superconductors to build functional devices and circuits, known as superconducting electronics [1], has developed for decades and spawned wide applications including superconducting circuits [2,3], superconducting quantum interference devices (SQUIDs) [4,5], and superconducting qubits [6,7]. Owing to the zero resistance and Meissner effect [8] of superconductors, superconducting devices exhibit superior advantages over their semiconducting counterparts, such as low loss, high sensitivity, and ultrafast operation speed. Josephson junctions (JJs) act as the building block of superconducting electronic devices and circuits. Embedding two JJs into a SQUID is one way to study the current phase relation (CPR) [9] and also produces magnetic field detectors with high sensitivity. Topological and nontopological phase transitions have been reported experimentally in HgTe quantum well [10,11], InAs [12], Bi_2Se_3 [13], and Bi nanowires (NWs) [14] by measuring the CPR of the SQUID. A supercurrent parity meter is also achieved based on SQUID incorporating InSb NWs [15].

A topological semimetal nanostructure provides an ideal platform to study the SQUID physics and superconducting electronics due to its intrinsic band topology [16–19] and convenient fabrication [20]. With helical topological surface states, Dirac semimetal NWs are predicted to host Majorana zero modes when coupled to *s*-wave superconductors [21–23]. Braiding operations of Majorana modes constitute logical gates of a topological quantum computer [24] and require an interconnected nanowire network [25]. The construction of SQUIDs based on Dirac semimetal NWs is a necessary step toward the final integration of NW networks with superconducting islands. Here we report the supercurrent transport measurements of a SQUID based on Cd_3As_2 NWs. As a paradigm of Dirac semimetals, Cd_3As_2 shows a linear energy dispersion around bulk Dirac nodes [26–30] and helical Fermi arc states on the surface [30–32]. The Cd_3As_2 NWs, with their large surface-to-volume ratio and easy field-effect gating, facilitate the observation of surface-related phenomena such as the π-Aharonov-Bohm (π-AB) effect [33,34], Fano interference [35], and topological transition of superconductivity [21,22].

In this work, we have fabricated a nearly symmetric SQUID that consists of two Nb-Cd_3As_2 NW-Nb JJs. Both the single JJ and SQUID show a gate-switchable on/off supercurrent from the electron to the hole branch. Under an out-of-plane perpendicular magnetic field, the critical current I_c of the SQUID shows an anomalous magnetic enhancement near the Dirac point, where surface states become manifest and *p*-wave superconductivity may take place. The supercurrent of the SQUID is also studied under in-plane magnetic fields at different directions, presenting a typical π-periodic variation with the rotation angle.

*chenjj3@sustech.edu.cn
†anqi0112@pku.edu.cn
‡liaozm@pku.edu.cn

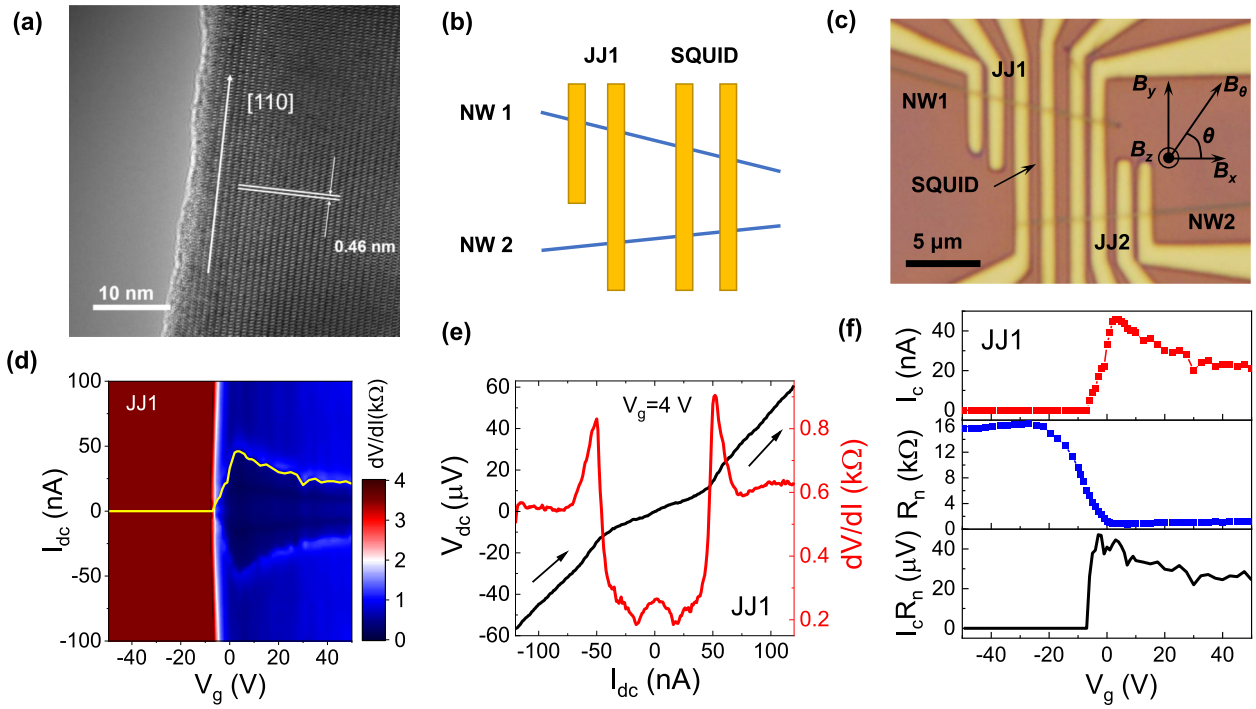

FIG. 1. Supercurrent FET in Nb-Cd_3As_2-Nb JJ. (a) High-resolution TEM image of a typical Cd_3As_2 nanowire with a [110] growth direction. (b) Configuration of the JJ and SQUID. Two nanowires (NW 1 and NW 2) are denoted by the blue lines, and the Nb/Pd electrodes are denoted by yellow stripes. (c) Optical image of the studied device. The channel length of JJ1 and JJ2 is ∼1 μm, while the loop area of the SQUID is $S \sim 14\ \mu m^2$. The B_x direction is defined as the angle bisector of the two NWs. (d) Color plot of dV/dI versus gate voltage V_g and current I_{dc} in JJ1 at 10 mK. The central dark region in the positive V_g side represents the superconducting phase, where its upper boundary indicates the critical current I_c, as shown by the yellow curve, exhibiting the supercurrent FET behavior. (e) The $I-V$ characteristic and the corresponding dV/dI spectrum at 10 mK, $V_g = 4$ V for JJ1. The black arrows denote the dc current sweeping direction. (f) Critical current I_c, normal resistance R_n (at $I_{dc} = 0.5$ μA), and the product of I_cR_n as a function of gate voltage V_g for JJ1.

II. MATERIALS AND METHODS

The same batch of Cd_3As_2 NWs grown by the chemical vapor deposition method [36] were used to fabricate the JJs and SQUID. The monocrystalline NWs were grown along the [110] direction, as revealed by the high-resolution transmission electron microscopy (TEM) image in Fig. 1(a). Two individual NWs, nanowire 1 (NW 1) and nanowire 2 (NW 2), as sketched in Fig. 1(b), were transferred to a silicon substrate with a 285-nm-thick SiO_2 layer serving as a back gate. The two NWs are placed at a relative angle of about 20°. After an *in situ* Ar ion etching process to remove the native oxide layer, a series of Nb (150-nm)/Pd (5-nm) electrodes with different spacings were deposited on the NWs by magnetron sputtering. As shown in Fig. 1(b), JJs and the SQUID are formed between different electrodes. Figure 1(c) shows the optical image of the device studied in this work, with JJ1, JJ2, and SQUID indicated. The channel length (i.e., separation between the superconducting electrodes) is ∼1 μm for JJ1 and JJ2, while the loop area of SQUID is ∼14 μm^2. Transport measurements were carried out in a dilution refrigerator with a base temperature of 10 mK. The differential resistance (dV/dI) was obtained by applying a dc current I_{dc} and a small ac excitation I_{ac} (1 nA) to the sample and simultaneously recording the ac voltage via the lock-in amplifier (SR830). All of the superconducting transport measurements were conducted in the four-probe (or pseudo-four-probe) current-voltage geometry. A three-axis vector magnet was used to produce magnetic fields in different directions.

III. RESULTS AND DISCUSSION

The property of a single JJ is first characterized. Figure 1(d) shows the color map of dV/dI versus gate voltage V_g and current I_{dc} for JJ1 at 10 mK. The central dark region in the positive V_g part represents the superconducting state, where its upper boundary gives the critical current I_c [denoted by the yellow curve in Fig. 1(d)]. The $I_c - V_g$ curve of JJ2 is nearly the same as that of JJ1, indicating the similar properties of the two NWs. As shown in Fig. 1(d), the nanowire junction demonstrates supercurrents in positive V_g regions. While the V_g is tuned below 0 V, the critical supercurrent drops drastically and reaches zero below $V_g = -7$ V. The gate-controlled on/off supercurrent largely originates from the asymmetric mobility of the two types of carriers in Cd_3As_2 NWs [22,23]. In JJ1, based on the transfer curve, the electron and hole mobility are estimated to be 1.16×10^5 and $83\ cm^2/(V\cdot s)$, respectively. Besides, the heavy electron doping near the Nb electrodes causes the formation of p-n barriers [23] in the junction for negative V_g. The divergent carrier mobility and the formed p-n wall together leads to the different superconducting behaviors at the electron and hole regions. The supercurrent is switched on/off as modulating V_g from

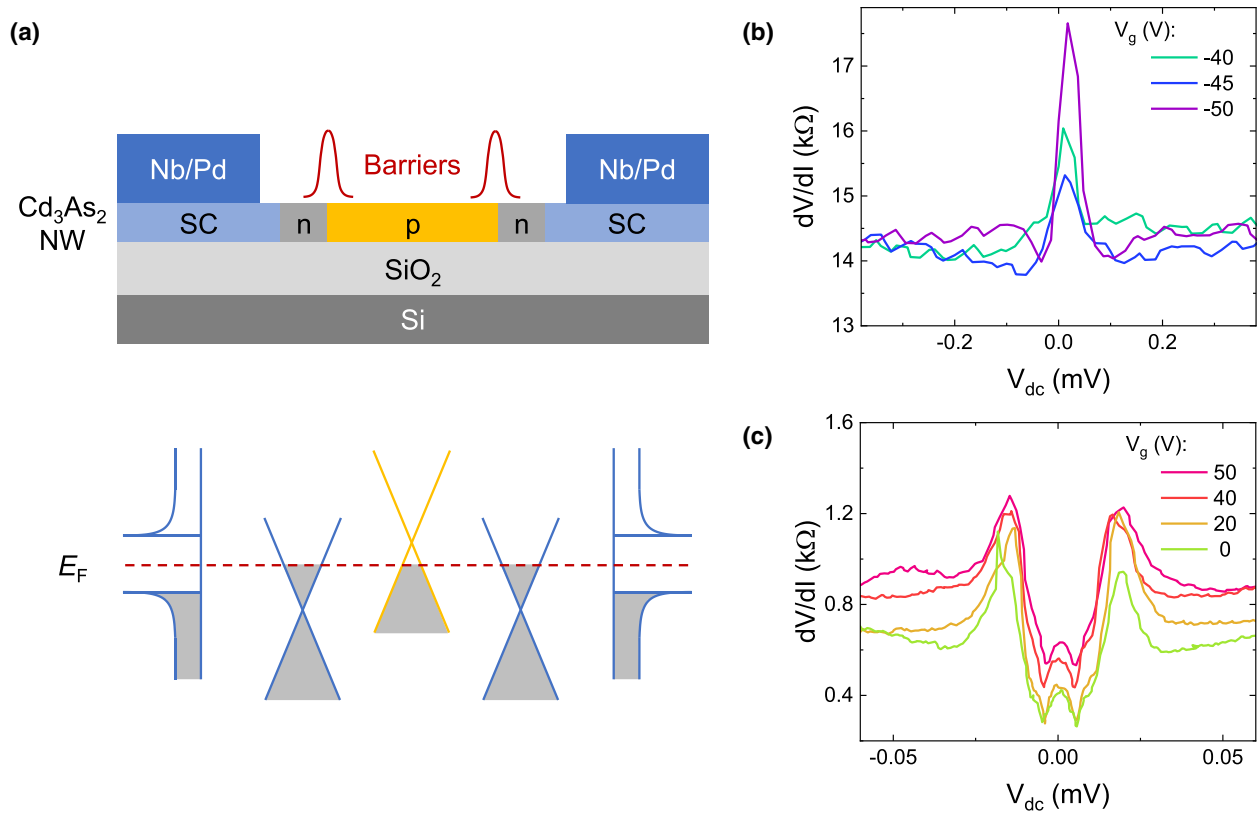

FIG. 2. Tunneling barriers formed due to heterogeneous doping in JJ1. (a) Top panel: device schematic with heterogeneous doping for negative V_g. Near the Nb contacts, the NW is heavily n-type doped, which is hardly tuned due to electrostatic screening. When $V_g < 0$, two effective p-n barriers are formed in the channel. Bottom panel: band diagram of the NW. (b) dV/dI versus V_{dc} for negative V_g. Large zero-bias resistance peaks are obtained. (c) dV/dI as a function of V_{dc} for positive V_g.

positive to negative. The Cd_3As_2 NWs provide a convenient and scalable platform to realize the electrically tuned supercurrent field-effect transistor (FET).

Another interesting observation is that for "on" state, $I_c - V_g$ displays a superconducting dome that shows a maximum I_c at around $V_g = 4$ V. The dome-shaped I_c was previously observed in Cd_3As_2-based JJs when the surface state superconductivity was prominent [23,37]. For the nanowire junction with channel length ∼1 μm here, the bulk superconductivity is suppressed, and the supercurrents are mainly carried by the surface state due to its topological nature and much longer coherence length [23]. When tuning the gate voltage V_g to positive, the Fermi level and the density of bulk states are increased. The enhanced bulk-surface interaction would lead to the dephasing of the superconducting state with reduced I_c at a larger V_g [23,38].

Figure 1(e) shows the current-voltage ($I-V$) curve and the corresponding differential resistance (dV/dI) spectrum of JJ1 at 10 mK and $V_g = 4\,V$. The I_{dc} was swept from negative to positive and the critical current I_c seen from Fig. 1(e) is about 45 nA. The dV/dI spectrum shows a residual resistance in the superconducting branch, which will be elaborated in the following paragraphs. Figure 1(f) shows the critical current I_c, normal resistance R_n (at $I_{dc} = 0.5$ μA), and I_cR_n result as a function of V_g (from −50 V to 50 V). The I_cR_n shows a maximum of 47.2 μV at $V_g = -3$ V.

To clarify the gate dependence of transport in nanowires further, we study the zero-bias resistance of JJ1 at different V_g. A sketch of the device configuration is shown in the top panel in Fig. 2(a). Near the Nb contacts, the nanowire is n-type doped [23] and the Fermi level could hardly be tuned by the back gate V_g due to the electrostatic screening effect. When applying a negative V_g, the Dirac point of the segment between the two Nb electrodes would be pushed upward above the Fermi level [39], as shown by the bottom panel in Fig. 2(a). An n-p-n junction is thus formed, with potential barriers located at the two p-n interfaces, which would greatly suppress the conductivity and result in the quench of supercurrents [Fig. 1(d)]. Sharp zero-bias resistance peaks are also clearly observed at negative voltages [Fig. 2(b)]. When increasing the bias voltage V_{dc}, the probability of carriers transmitting the p-n interface is enhanced and gives rise to a resistance drop. The largest zero-bias resistance peak occurs at the lowest gate voltage ($V_g = -47$ V), where the Dirac point of the middle segment of NW 1 is shifted far above the Fermi energy. For $V_g > 0$, the whole nanowire is an n-type doped open system where no tunnel barrier is expected [39]. However, as shown in Fig. 2(c), the nanowire exhibits a residual resistance peak (several hundred Ohms) at zero bias, suggesting incomplete superconductivity. This partial superconducting state may arise from the existence of a potential barrier induced by defect states or impurities in the nanowire channel. Upon lifting

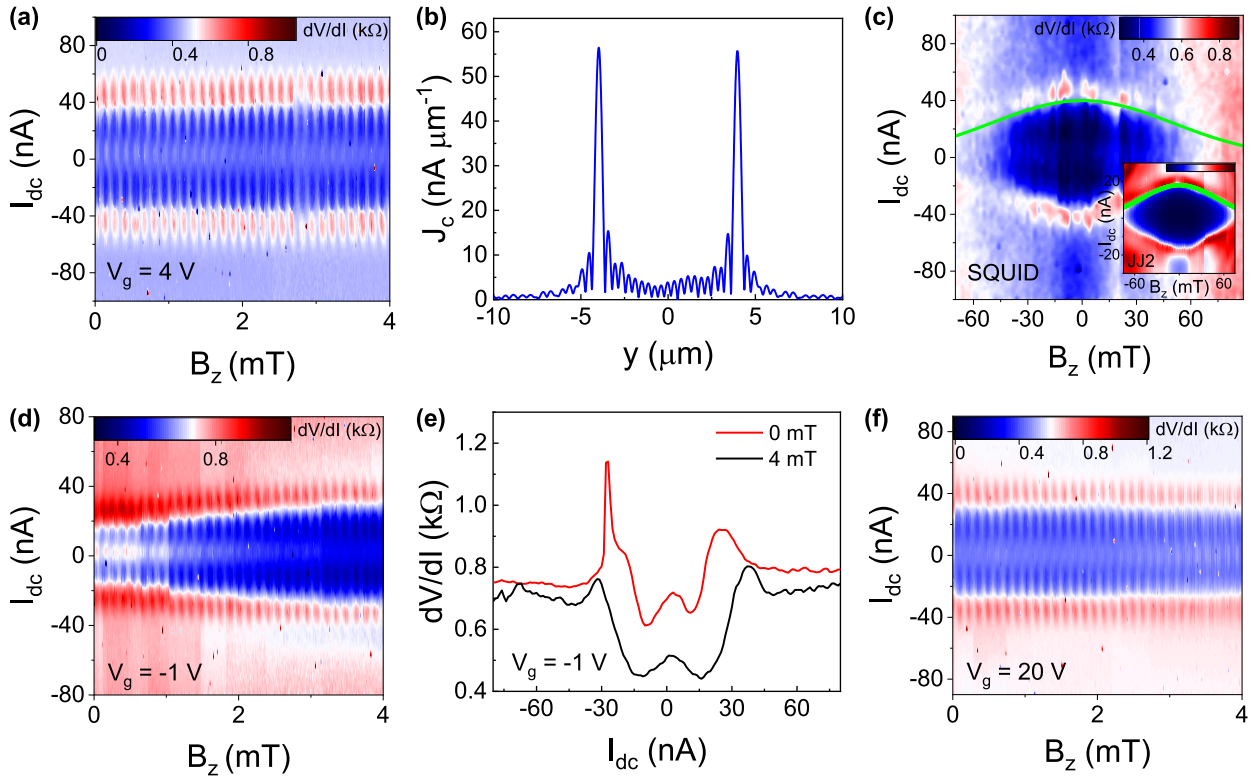

FIG. 3. Magnetic modulation of supercurrents in the SQUID under an out-of-plane perpendicular field. (a) dV/dI as a function of B_z and I_{dc} at $V_g = 4$ V. (b) The corresponding supercurrent density profile $J_c(y)$ of the $I_c(B_z)$ data extracted from (a). (c) dV/dI at a larger magnetic field ($V_g = 4$ V). The green curve is the Gaussian fitting of $I_c - B_z$ with a decaying coefficient σ of 50 mT. Inset: dV/dI mapping of JJ2. Gaussian fitting of the $I_c - B_z$ decaying is depicted by the green curve. The decaying coefficient σ is fitted to be 50 mT. (d) dV/dI as a function of B_z and I_{dc} at $V_g = -1$ V (near the Dirac point). (e) dV/dI versus I_{dc} for 0 and 4 mT extracted from (d). (f) dV/dI as a function of B_z and I_{dc} at $V_g = 20$ V.

the V_{dc}, a resistance drop is observed due to overcoming the potential barrier, similar to the case in Fig. 2(b). In addition, the imperfect nanowire-superconductor interface, insufficient filtering, and inevitable noise from the environment may also play a role in the observation of residual resistance.

We next study the magnetic responses of the SQUID under different gate voltages. Since the critical currents of JJ1 and JJ2 are almost identical, a symmetric SQUID is expected. In Fig. 3(a), the dV/dI mapping shows an obvious $I_c - B_z$ oscillation from 0 to 4 mT measured at $V_g = 4$ V. Indeed, the $I_c - B_z$ oscillation is equally periodic and does not decay in 0 to 4 mT as expected for a symmetric SQUID. The periodicity of the I_c oscillation is extracted to be $\Delta B_z = 0.135$ mT. From the flux quantum $\Phi_0 = \Delta B \cdot S$, the area of the SQUID loop is estimated to be 15 μm^2, close to the actual geometric area (∼14 μm^2). The magnetic penetration depth λ of the Nb electrodes is calculated to be about 470 nm from $S = (L + 2\lambda)W$, where L is the length of the SQUID and W is the width of the SQUID. The feature of symmetric SQUID is further proved by the calculated supercurrent density distribution $J_c(y)$ in Fig. 3(b). The corresponding $J_c(y)$ shows two nearly identical peaks localized 8 μm away from each other, well consistent with the actual distance between the two NWs.

When increasing the magnetic field to larger values, the envelope of critical current in the SQUID demonstrates a monotonous decay with B_z. Figure 3(c) shows the overall evolution of dV/dI versus I_{dc} and B_z. The decaying I_c can be fitted by the Gaussian function $I_c(B_z) \approx I_c(0)e^{-\frac{B_z^2}{2\sigma^2}}$ [green curve in Fig. 3(c)], where the obtained decaying coefficient σ is 50 mT. The inset of Fig. 3(c) shows the dV/dI mapping of a single NW-based junction, where a Gaussian-like decay of I_c is also observed. For $B_z < 60$ mT, the magnetic length $\xi_B = \sqrt{\Phi_0/B_z} > 186$ nm is larger than the nanowire junction width W (∼100 nm), where the narrow junction model applies and the I_c can be fitted by the Gaussian function [23,40,41]. The Gaussian fitting yields a decaying coefficient σ of 50 mT—identical to that of the SQUID. Thus, the reduction of I_c in the SQUID at higher fields should arise from the magnetic reduction of the supercurrent in the single NW junction.

When the gate voltage is tuned near the Dirac point [Fig. 3(d)], the SQUID exhibits an anomalous field-enhanced superconductivity behavior. The envelope of critical current I_c, at which the device is switched from the supercurrent branch (blue region) to the normal one (red region), is enhanced upon the increment of B_z. As shown in Fig. 3(e), the SQUID becomes less resistive and more superconducting, as indicated by the drop of zero-bias resistance, when lifting B_z from 0 to 4 mT. The gate-tuned experiment shows that the supercurrent enhancement only appears at $V_g = -1$ V (near the Dirac point), but is absent at other gates [Fig. 3(a) and 3(f)]. The magnetic field-enhanced superconductivity itself is an

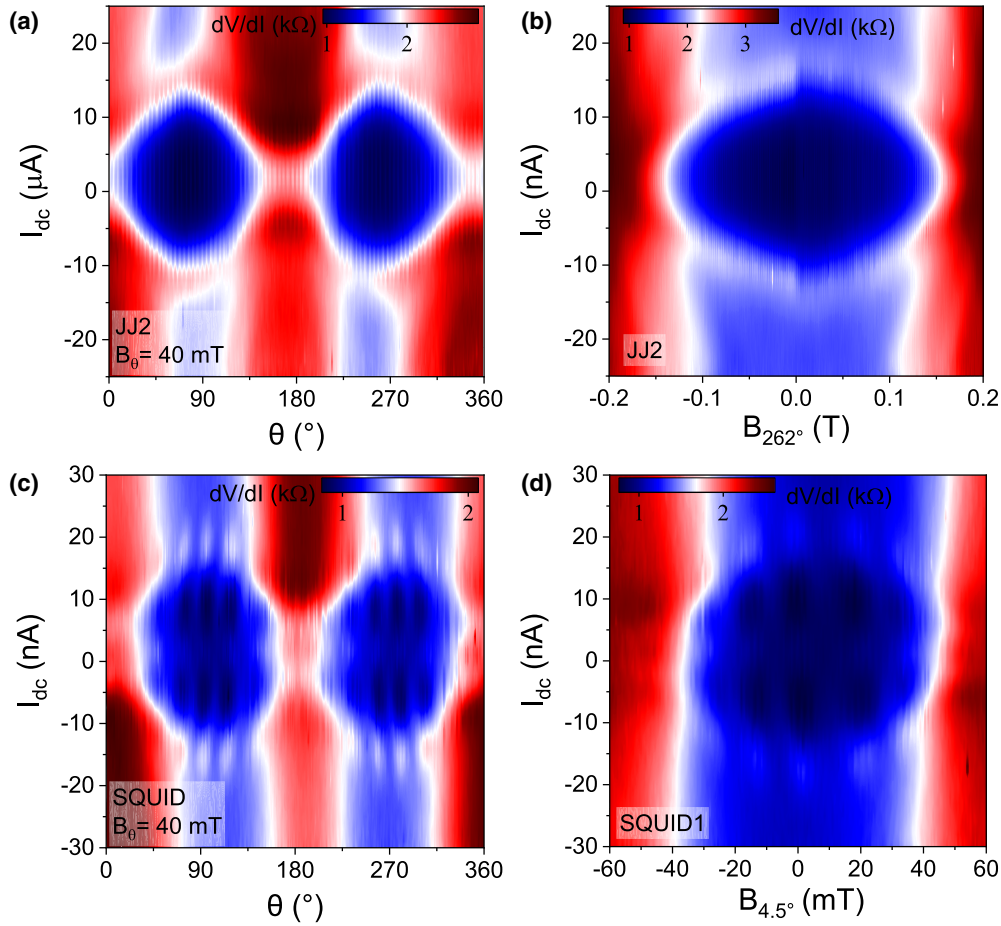

FIG. 4. Critical currents of JJ2 and the SQUID under in-plane magnetic fields. (a) dV/dI mapping with an in-plane magnetic field $B_\theta = 40$ mT in JJ2 ($V_g = 0$ V). θ is defined as the relative angle between the magnetic field and B_x [Fig. 1(c)]. (b) dV/dI mapping under an in-plane magnetic field with $\theta = 262^\circ$ in JJ2 ($V_g = 0$ V). (c) dV/dI mapping with an in-plane magnetic field $B_\theta = 40$ mT in the SQUID ($V_g = 1$ V). (d) dV/dI mapping under an in-plane magnetic field with $\theta = 4.5^\circ$ in the SQUID ($V_g = 1$ V).

interesting phenomenon, and here we discuss possible mechanisms for it. During our measurements, the enhancement is reproducible by varying magnetic field sweep rates, and it appears at both a positive and negative magnetic field, excluding the influence of measurement error and magnetic field offset. The magnetic flux focusing and misalignment could possibly lead to the increasing I_c upon applying magnetic fields. If there is any, it should cause a similar supercurrent enhancement despite different gates, which is obviously not the case in our work. Therefore, the flux focusing and field misalignment can be safely ruled out. Indeed, the enhancement takes place near the Dirac point, where the bulk density of states is minimized and the topological surface states become manifest. As reported in Ref. [42], the topological surface states coupled to an s-wave superconductor would give birth to unconventional p-wave superconductivity, which would result in an I_c dip at $B = 0$, especially when the interface transparency is low. Here in our work, the formation of p-n junctions when $V_g < 0$ would induce a low interface transparency and facilitate the observation of I_c enhancement at finite magnetic fields. However, more experimental and theoretical efforts are required in the future to ascertain the existence of p-wave superconductivity.

We further study the in-plane magnetic field effect on JJ2 and the SQUID. The angular dependence of the critical current for JJ2 is measured at a fixed field amplitude in different directions [Fig. 4(a)]. The critical current displays a π periodicity. When the magnetic field is parallel or antiparallel to the current flow ($\theta \approx 0^\circ$ or 180°), the critical current obtains the minimum. When the magnetic field is perpendicular to the current flow ($\theta = 262^\circ$), the critical current shows a maximum of 14 nA. This suggests that the decaying rate of the supercurrent is dependent on the in-plane magnetic field direction. The behavior might result from different amounts of effective magnetic flux threading the NW when the magnetic field is in-plane rotated. JJ2 is then measured at $\theta = 262^\circ$. The supercurrent persists up to a critical magnetic field as large as $\sim$150 mT [Fig. 4(b)]. The in-plane magnetic field rotation experiment is also performed in the SQUID. dV/dI of the SQUID is shown in Fig. 4(c) ($B_\theta = 40$ mT, $V_g = 1$ V). The envelope of I_c shows a similar behavior as JJ2. Inside the envelope, some fast oscillations can be captured, which may result from the interference effect of the SQUID. Figure 4(d) shows the dV/dI mapping of the SQUID at $\theta = 4.5^\circ$. Similarly, fast oscillations with a period of $\sim$17 mT appear inside the superconducting region, which is absent in the single JJ.

The fast oscillation may originate from the SQUID geometry. Since the substrate might not be strictly horizontal, an out-of-plane component of the applied magnetic field is inevitable. Considering the period of $\Delta B_z = 0.135$ mT [Fig. 3], a 0.5 ° tilt of the substrate can induce a considerable out-of-plane magnetic field component that will cause a SQUID oscillation with an in-plane period of ∼17 mT inside the envelope of I_c.

IV. CONCLUSION

In conclusion, we have fabricated Nb-Cd_3As_2-Nb-based JJs and a SQUID. The JJs exhibit gate-switchable supercurrents, providing a promising platform for developing a Josephson supercurrent FET. In the presence of an out-of-plane magnetic field, the I_c envelope of the SQUID demonstrates an anomalous field enhancement near the Dirac point. Besides, the SQUID shows a typical π periodicity of a critical current with respect to the in-plane field direction. This work demonstrates the ability to manufacture Cd_3As_2 NW-based JJs and a SQUID with arbitrary geometry, paving the way for designing and building the topological NW-superconductor-based superconducting quantum circuits, which is significant for realizing Majorana quantum state braiding.

ACKNOWLEDGMENTS

This work was supported by the Key-Area Research and Development Program of Guangdong Province (Grant No. 2020B0303060001), the National Natural Science Foundation of China (Grants No. 91964201, No. 61825401, and No. 12204016), the China Postdoctoral Science Foundation (Grant No. 2021M700254), and the Innovation Program for Quantum Science and Technology (Grant No. 2021ZD0302403).

[1] A. I. Braginski, Superconductor electronics: Status and outlook, J. Supercond. Novel Magn. **32**, 23 (2018).

[2] M. H. Devoret and R. J. Schoelkopf, Superconducting circuits for quantum information: An outlook, Science **339**, 1169 (2013).

[3] G. Wendin, Quantum information processing with superconducting circuits: A review, Rep. Prog. Phys. **80**, 106001 (2017).

[4] R. L. Fagaly, Superconducting quantum interference device instruments and applications, Rev. Sci. Instrum. **77**, 101101 (2006).

[5] C. Granata and A. Vettoliere, Nano superconducting quantum interference device: A powerful tool for nanoscale investigations, Phys. Rep. **614**, 1 (2016).

[6] J. Clarke and F. K. Wilhelm, Superconducting quantum bits, Nature (London) **453**, 1031 (2008).

[7] M. Kjaergaard, M. E. Schwartz, J. Braumüller, P. Krantz, J. I. J. Wang, S. Gustavsson, and W. D. Oliver, Superconducting qubits: Current state of play, Annu. Rev. Condens. Matter Phys. **11**, 369 (2020).

[8] D. van Delft and P. Kes, The discovery of superconductivity, Phys. Today **63**(9), 38 (2010).

[9] A. A. Golubov, M. Y. Kupriyanov, and E. Il'ichev, The current-phase relation in Josephson junctions, Rev. Mod. Phys. **76**, 411 (2004).

[10] S. Hart, H. Ren, M. Kosowsky, G. Ben-Shach, P. Leubner, C. Brüne, H. Buhmann, L. W. Molenkamp, B. I. Halperin, and A. Yacoby, Controlled finite momentum pairing and spatially varying order parameter in proximitized HgTe quantum wells, Nat. Phys. **13**, 87 (2016).

[11] H. Ren, F. Pientka, S. Hart, A. T. Pierce, M. Kosowsky, L. Lunczer, R. Schlereth, B. Scharf, E. M. Hankiewicz, L. W. Molenkamp, B. I. Halperin, and A. Yacoby, Topological superconductivity in a phase-controlled Josephson junction, Nature (London) **569**, 93 (2019).

[12] W. Mayer, M. C. Dartiailh, J. Yuan, K. S. Wickramasinghe, E. Rossi, and J. Shabani, Gate controlled anomalous phase shift in Al/InAs Josephson junctions, Nat. Commun. **11**, 212 (2020).

[13] A. Assouline, C. Feuillet-Palma, N. Bergeal, T. Zhang, A. Mottaghizadeh, A. Zimmers, E. Lhuillier, M. Eddrie, P. Atkinson, M. Aprili, and H. Aubin, Spin-orbit induced phase-shift in Bi_2Se_3 Josephson junctions, Nat. Commun. **10**, 126 (2019).

[14] A. Murani, A. Kasumov, S. Sengupta, Y. A. Kasumov, V. T. Volkov, I. I. Khodos, F. Brisset, R. Delagrange, A. Chepelianskii, R. Deblock, H. Bouchiat, and S. Gueron, Ballistic edge states in bismuth nanowires revealed by SQUID interferometry, Nat. Commun. **8**, 15941 (2017).

[15] J.-Y. Wang, C. Schrade, V. Levajac, D. van Driel, K. Li, S. Gazibegovic, G. Badawy, R. L. M. Op het Veld, J. S. Lee, M. Pendharkar, C. P. Dempsey, C. J. Palmstrøm, E. P. A. M. Bakkers, L. Fu, L. P. Kouwenhoven, and J. Shen, Supercurrent parity meter in a nanowire Cooper pair transistor, Sci. Adv. **8**, eabm9896 (2022).

[16] N. P. Armitage, E. J. Mele, and A. Vishwanath, Weyl and Dirac semimetals in three-dimensional solids, Rev. Mod. Phys. **90**, 015001 (2018).

[17] A. A. Burkov, Topological semimetals, Nat. Mater. **15**, 1145 (2016).

[18] S. Wang, B.-C. Lin, A.-Q. Wang, D.-P. Yu, and Z.-M. Liao, Quantum transport in Dirac and Weyl semimetals: A review, Adv. Phys.: X **2**, 518 (2017).

[19] A.-Q. Wang, X.-G. Ye, D.-P. Yu, and Z.-M. Liao, Topological semimetal nanostructures: From properties to topotronics, ACS Nano **14**, 3755 (2020).

[20] P. Liu, J. R. Williams, and J. J. Cha, Topological nanomaterials, Nat. Rev. Mater. **4**, 479 (2019).

[21] A. Q. Wang, C. Z. Li, C. Li, Z. M. Liao, A. Brinkman, and D. P. Yu, 4π-Periodic Supercurrent from Surface States in Cd_3As_2 Nanowire-Based Josephson Junctions, Phys. Rev. Lett. **121**, 237701 (2018).

[22] C.-Z. Li, A.-Q. Wang, C. Li, W.-Z. Zheng, A. Brinkman, D.-P. Yu, and Z.-M. Liao, Topological Transition of Superconductivity in Dirac Semimetal Nanowire Josephson Junctions, Phys. Rev. Lett. **126**, 027001 (2021).

[23] C.-Z. Li, C. Li, L.-X. Wang, S. Wang, Z.-M. Liao, A. Brinkman, and D.-P. Yu, Bulk and surface states carried supercurrent in

ballistic Nb-Dirac semimetal Cd_3As_2 nanowire-Nb junctions, Phys. Rev. B **97**, 115446 (2018).

[24] S. D. Sarma, M. Freedman, and C. Nayak, Majorana zero modes and topological quantum computation, npj Quantum Inf. **1**, 15001 (2015).

[25] T. Karzig, C. Knapp, R. M. Lutchyn, P. Bonderson, M. B. Hastings, C. Nayak, J. Alicea, K. Flensberg, S. Plugge, Y. Oreg, C. M. Marcus, and M. H. Freedman, Scalable designs for quasiparticle-poisoning-protected topological quantum computation with Majorana zero modes, Phys. Rev. B **95**, 235305 (2017).

[26] Z. Wang, Y. Sun, X.-Q. Chen, C. Franchini, G. Xu, H. Weng, X. Dai, and Z. Fang, Dirac semimetal and topological phase transitions in A_3Bi (A = Na, K, Rb), Phys. Rev. B **85**, 195320 (2012).

[27] Z. Wang, H. Weng, Q. Wu, X. Dai, and Z. Fang, Three-dimensional Dirac semimetal and quantum transport in Cd_3As_2, Phys. Rev. B **88**, 125427 (2013).

[28] Z. K. Liu, J. Jiang, B. Zhou, Z. J. Wang, Y. Zhang, H. M. Weng, D. Prabhakaran, S. K. Mo, H. Peng, P. Dudin, T. Kim, M. Hoesch, Z. Fang, X. Dai, Z. X. Shen, D. L. Feng, Z. Hussain, and Y. L. Chen, A stable three-dimensional topological Dirac semimetal Cd_3As_2, Nat. Mater. **13**, 677 (2014).

[29] M. Neupane, S.-Y. Xu, R. Sankar, N. Alidoust, G. Bian, C. Liu, I. Belopolski, T.-R. Chang, H.-T. Jeng, H. Lin, A. Bansil, F. Chou, and M. Z. Hasan, Observation of a three-dimensional topological Dirac semimetal phase in high-mobility Cd_3As_2, Nat. Commun. **5**, 3786 (2014).

[30] S. Jeon, B. B. Zhou, A. Gyenis, B. E. Feldman, I. Kimchi, A. C. Potter, Q. D. Gibson, R. J. Cava, A. Vishwanath, and A. Yazdani, Landau quantization and quasiparticle interference in the three-dimensional Dirac semimetal Cd_3As_2, Nat. Mater. **13**, 851 (2014).

[31] S.-Y. Xu, C. Liu, S. K. Kushwaha, R. Sankar, J. W. Krizan, I. Belopolski, M. Neupane, G. Bian, N. Alidoust, T.-R. Chang, H.-T. Jeng, C.-Y. Huang, W.-F. Tsai, H. Lin, P. P. Shibayev, F.-C. Chou, R. J. Cava, and M. Z. Hasan, Observation of Fermi arc surface states in a topological metal, Science **347**, 294 (2015).

[32] S.-Y. Xu *et al.*, Discovery of a Weyl fermion semimetal and topological Fermi arcs, Science **349**, 613 (2015).

[33] L.-X. Wang, C.-Z. Li, D.-P. Yu, and Z.-M. Liao, Aharonov–Bohm oscillations in Dirac semimetal Cd_3As_2 nanowires, Nat. Commun. **7**, 10769 (2016).

[34] B.-C. Lin, S. Wang, L.-X. Wang, C.-Z. Li, J.-G. Li, D. Yu, and Z.-M. Liao, Gate-tuned Aharonov-Bohm interference of surface states in a quasiballistic Dirac semimetal nanowire, Phys. Rev. B **95**, 235436 (2017).

[35] S. Wang, B.-C. Lin, W.-Z. Zheng, D. Yu, and Z.-M. Liao, Fano Interference between Bulk and Surface States of a Dirac Semimetal Cd_3As_2 Nanowire, Phys. Rev. Lett. **120**, 257701 (2018).

[36] C.-Z. Li, R. Zhu, X. Ke, J.-M. Zhang, L.-X. Wang, L. Zhang, Z.-M. Liao, and D. Yu, Synthesis and photovoltaic properties of Cd_3As_2 faceted nanoplates and nano-octahedrons, Cryst. Growth Des. **15**, 3264 (2015).

[37] C. Z. Li, A. Q. Wang, C. Li, W. Z. Zheng, A. Brinkman, D. P. Yu, and Z. M. Liao, Reducing Electronic Transport Dimension to Topological Hinge States by Increasing Geometry Size of Dirac Semimetal Josephson Junctions, Phys. Rev. Lett. **124**, 156601 (2020).

[38] J. Liao, Y. Ou, H. Liu, K. He, X. Ma, Q.-K. Xue, and Y. Li, Enhanced electron dephasing in three-dimensional topological insulators, Nat. Commun. **8**, 16071 (2017).

[39] M. Jung, K. Yoshida, K. Park, X.-X. Zhang, C. Yesilyurt, Z. B. Siu, M. B. A. Jalil, J. Park, J. Park, N. Nagaosa, J. Seo, and K. Hirakawa, Quantum dots formed in three-dimensional Dirac semimetal Cd_3As_2 nanowires, Nano Lett. **18**, 1863 (2018).

[40] F. Chiodi, M. Ferrier, S. Guéron, J. C. Cuevas, G. Montambaux, F. Fortuna, A. Kasumov, and H. Bouchiat, Geometry-related magnetic interference patterns in long SNS Josephson junctions, Phys. Rev. B **86**, 064510 (2012).

[41] J. C. Cuevas and F. S. Bergeret, Magnetic Interference Patterns and Vortices in Diffusive SNS Junctions, Phys. Rev. Lett. **99**, 217002 (2007).

[42] S. Charpentier, L. Galletti, G. Kunakova, R. Arpaia, Y. Song, R. Baghdadi, S. M. Wang, A. Kalaboukhov, E. Olsson, F. Tafuri, D. Golubev, J. Linder, T. Bauch, and F. Lombardi, Induced unconventional superconductivity on the surface states of Bi_2Te_3 topological insulator, Nat. Commun. **8**, 2019 (2017).